The International Journal of Advanced Manufacturing Technology (2020) 106:3975–3984
https://doi.org/10.1007/s00170-019-04897-3

ORIGINAL ARTICLE

Surface topography model with considering corner radius and diameter of ball-nose end miller

Jing Zhang[1,2] · Song Zhang[1,2] · Dongdong Jiang[1,2] · Jiachang Wang[3] · Shaolei Lu[3]

Received: 4 April 2019 / Accepted: 23 December 2019 / Published online: 10 January 2020

Abstract
Surface topography, as one of the significant roles in surface integrity, has a great impact on the performances and service life of the machined parts. This research focuses on the surface topography model for the ball-nose end miller in machining of AISI P20 steel. First, the model is developed to predict the surface topography and surface roughness in ball-nose end milling process. Secondly, the accuracy of the developed surface topography model was verified by a series of milling experiments. Thirdly, the effects of corner radius and diameter of ball-nose end miller on surface roughness is analyzed, it is observed that the ratio of feed per tooth (f_z) to radial depth of cutting (a_e) for obtaining minimum surface roughness is related to the ratio of diameter (D) to corner radius (r) of ball-nose end miller. Finally, in terms of the minimum surface roughness, a mathematical model is established with consideration of corner radius and diameter of ball-nose end miller. This research indicates that proper selection of cutting parameters (f_z and a_e) with consideration of diameter and radius corner of ball-nose end miller is a novel avenue for acquiring desired surface roughness.

Keywords Surface topography · Ball-nose end miller · Ratio of feed per tooth to radial depth of cutting · Ratio of diameter to corner radius of cutter

Abbreviations

f_z	Feed per tooth (mm/tooth)
a_e	Radial depth of cutting (mm)
v_c	Cutting speed (m/min)
a_p	Axial depth of cutting (mm)
r	Corner radius of ball-nose end miller (mm)
R	Radius of ball-nose end miller (mm)
D	Diameter of ball-nose end miller (mm)
S_a	Three-dimensional arithmetic average deviation (μm)
C	Ratio of feed per tooth to radial depth of cutting
T_1, T_2	Coordinate transformation matrixes
P	Arbitrary point on the cutting edge
x, y, z	Coordinate of point P in workpiece coordinate system
u, v, w	Coordinate of point P in cutting tool coordinate system
x_0, y_0, z_0	Initial position of point P
β_1, β_2	Rotation angles of tool coordinate system around the X-axis and Z-axis of workpiece coordinate system, respectively
O_T-UVW	Tool coordinate system
O_W-XYZ	Workpiece coordinate system
γ	Helix angle of cutter
α	Angle between the O_TP and W-axis
ψ	Lag angle of point P
$R(\alpha)$	Radius of point P
H	Matrix consists of the points coordinates in workpiece model
m	Number of the mesh along the feed direction in workpiece model

✉ Song Zhang
zhangsong@sdu.edu.cn

1 Key Laboratory of High Efficiency and Clean Mechanical Manufacture of MOE, School of Mechanical Engineering, Shandong University, Jinan 250061, People's Republic of China

2 Key National Demonstration Center for Experimental Mechanical Engineering Education, Shandong University, Jinan 250061, People's Republic of China

3 Qingdao Hisense Mould Co., Ltd, Qingdao 266071, People's Republic of China

n Number of the mesh along the step-over direction in workpiece model

1 Introduction

With the development of modern manufacturing technology, the requirement for excellent surface integrity of the mold components is becoming higher and higher. Surface topography, as one of the main contents of surface integrity, has significant effect on wear resistance and fatigue resistance of the machined components. Accordingly, surface roughness is widely used as an index to evaluate the machined surface quality, in most cases, as a technical requirement for mechanical products [1–5]. Therefore, simulations of machined surface topography constitute an active research topic in the manufacturing community [6, 7].

In the last two decades, many researchers have been conducted to investigate the influence of geometric characteristic of milling process on surface topography, such as cutting parameters, tool path strategy, and inclined angle. Buj-Corral et al. [8] developed a model to predict the surface topography and surface roughness; the effects of feed rate, eccentricity as well as helix angle on surface roughness were analyzed in side milling process. Chen et al. [9] reported a new surface topography model that the path-interval and feed-interval scallops generating mechanism were described in the ball-end milling process. Both Erkorkmaz et al. [10] and Buj-Corral et al. [11] investigated the influence of feed rate on surface topography. In addition, Toh et al. [12] and Tam et al. [13] devoted to optimize the path strategy to improve the productivity and surface quality. Chen et al. [14] reported the effect of tool postures included title angle and lead angle on surface topography, it indicated that the scallop height has no relation to the inclination angles of the ball-end miller when only the spherical part of the cutter participates in the cutting process. Chen et al. [15] experimentally investigated the effect of inclination angle of cutting tool on cutting force, cutting temperature, and residual stress, which suggested that priority selection of inclination angle in feed direction can reduce the cutting force. Li et al. [16] established the surface topography model of the end milling by meshing the workpiece and discretizing the cutting edge, the relationship between the residual heights, cutting parameters, and diameter of cutter was investigated. Based on the trajectory equations of cutting edge relative to workpiece, Gao et al. [6] reported that a simplified model for predicting the machined surface was proposed without discretizing the cutting edge and meshing workpiece in ball-end milling process, and the influence of milling parameters on surface roughness was also analyzed. Quinsat et al. [17] proposed a simulated model of 3D topography for three-axis machining using a ball-end cutter; the feed rate and path-interval scallops were taken into consideration. Furthermore, some researchers developed a geometric model of machined surface for predicting the topography and surface roughness taking into account the tool vibration. Surmann et al. [18, 19] explored the mechanism of tool vibration in milling process, which indicated that it is further accurate to predict the surface topography with the knowledge of vibration trajectories of milling tools. Arizmendi et al. [20] proposed a surface topography model by taking account of the effect of tool vibrations on the equations of the cutting-edge paths. Toh [21] reported the investigation on surface topography analysis relating to cutter path orientations in the high-speed finish milling inclined hard steel. Wang et al. [22] proposed a mathematical model for predicting the surface topography and surface roughness in five-axis ball-end milling process, at the same time, the influence of tool inclination and feed rate as well as radial cutting depth on surface roughness was analyzed. Zhang et al. [23] developed an optimizing model of surface topography in ball-end milling of AISI H13 steel, which indicated that better surface topography can be obtained by employing the lower material remove rate. In addition, according to De Souza et al. [24], the effective tool diameter of ball-end mill in some case varies according to the axial depth of cutting, the tool nominal diameter, surface curvature, which can cause the surface topography to vary constantly. Likewise, the corner radius of cutting tool plays an important role in surface topography formation at different inclined angle of workpiece in milling process.

With the improvement of requirement for surface quality and machining efficiency, the ball-nose end miller is widely employed in mold machining. However, only a few studies have focused on the surface topography in ball-nose end milling process. In addition, the researches which take into account the effect of corner radius and diameter of ball-nose end miller on roughness when the cutting parameters are optimized to obtain the desired surface roughness are relatively scant.

Therefore, the main objective of this research is to predict the surface topography and optimize the cutting parameters for obtaining desired surface roughness. First, the theoretical model of surface topography formation in ball-nose end milling process was developed. Then, ball-nose end milling experiments were carried out to validate the availability of surface topography model. Furthermore, the effect of corner radius and diameter of ball-nose end miller on surface roughness is analyzed. Finally, in terms of the minimum surface roughness, a mathematical model was presented by considering of the corner radius and diameter of ball-nose end miller, which was also verified by a series of experiments.

2 Surface topography model

2.1 Motion equation of cutting edge

During cutting process, surface topography is the result of the relative motion of cutting-edge and workpiece surface. Figure 1 shows the schematic of machining coordinate systems, where the XY plane of workpiece coordinate system O_W-XYZ is parallel to the machined surface. Besides, the cutting tool coordinate system is fixed on the cutting tool, which rotates around the spindle with a velocity n. Based on the geometric relationship between the workpiece coordinate system and cutting tool system, the motion of discrete cutting-edge point can be expressed by Eq. (1),

$$P(x,y,z) = \begin{pmatrix} x \\ y \\ z \\ 1 \end{pmatrix} = T_1 T_2 \begin{pmatrix} u \\ v \\ w \\ 1 \end{pmatrix} \tag{1}$$

where P (x, y, z) and (u, v, w) are the coordinates of cutting-edge point in the workpiece coordinate system and tool coordinate system, respectively. T_1 and T_2 are the coordinate transformation matrixes, respectively. T_1 is the coordinate transformation matrix from the cutting tool coordinate system to the workpiece coordinate system and T_2 is the coordinate transformation matrix from the tool rotary coordinate to the tool kinematic coordinate, which can be given by Eqs. (2) and (3),

$$T_1 = \begin{pmatrix} \cos\beta_2 & \cos\beta_1\sin\beta_2 & -\sin\beta_1\sin\beta_2 & x_0 + (i-1)a_e \\ -\sin\beta_2 & \cos\beta_1\cos\beta_2 & -\sin\beta_1\cos\beta_2 & y_0 + \frac{n z_n f_z}{60} t \\ 0 & \sin\beta_1 & \cos\beta_1 & z_0 \\ 0 & 0 & 0 & 1 \end{pmatrix} \tag{2}$$

$$T_2 = \begin{pmatrix} \cos\left(\varphi_0 - \frac{2\pi n}{60} t\right) & -\sin\left(\varphi_0 - \frac{2\pi n}{60} t\right) & 0 & 0 \\ \sin\left(\varphi_0 - \frac{2\pi n}{60} t\right) & \cos\left(\varphi_0 - \frac{2\pi n}{60} t\right) & 0 & 0 \\ 0 & 1 & 1 & -R \\ 0 & 0 & 0 & 1 \end{pmatrix} \tag{3}$$

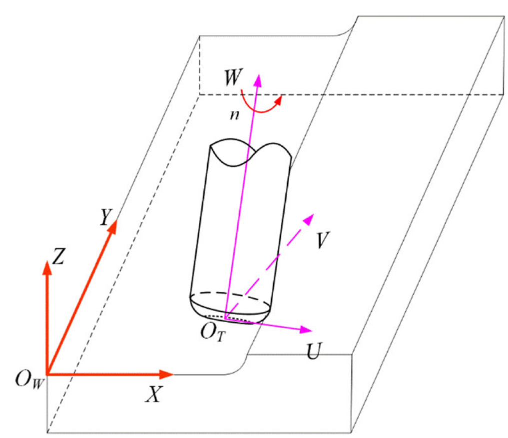

Fig. 1 Schematic of coordinate systems

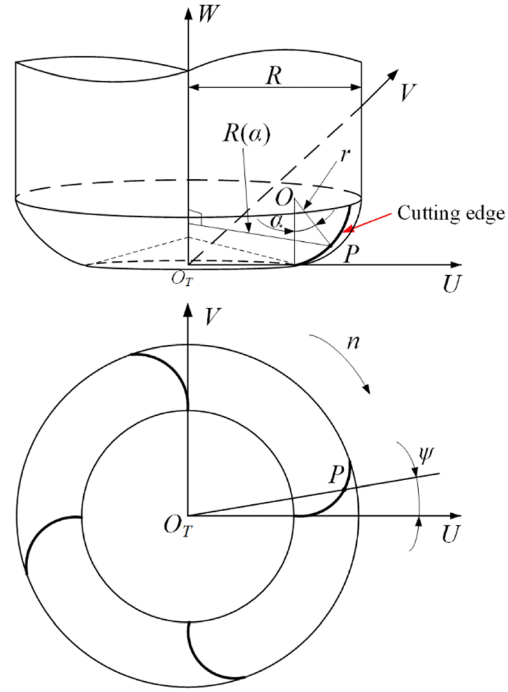

Fig. 2 Schematic of ball-nose end miller in tool coordinate system

where β_1 and β_2 denote the rotation angles of tool coordinate system around the X-axis and Z-axis of workpiece coordinate system, respectively. (x_0, y_0, z_0) denotes the initial position of point P, a_e is radial depth of cut, n is spindle speed, z_n is number of cutting edge, f_z is feed per tooth, i represents the number of tool path, and t is the cutting time during ith tool paths. φ_0 is the initial phase angle of cutting tool and R is the radius of cutting tool.

As shown in Fig. 2, the cutting edge of ball-nose end miller is described in tool coordinate system. For ball-nose end miller, the discrete cutting edge has the lag

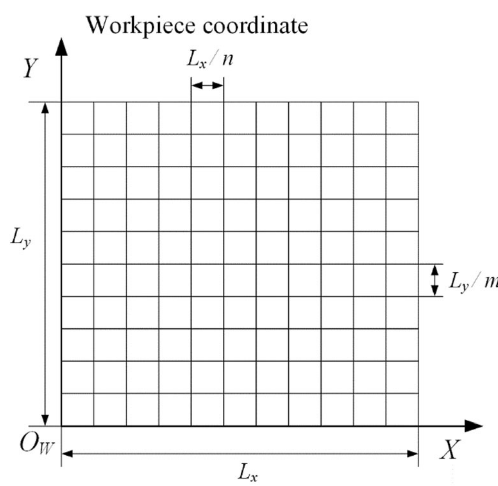

Fig. 3 Workpiece model

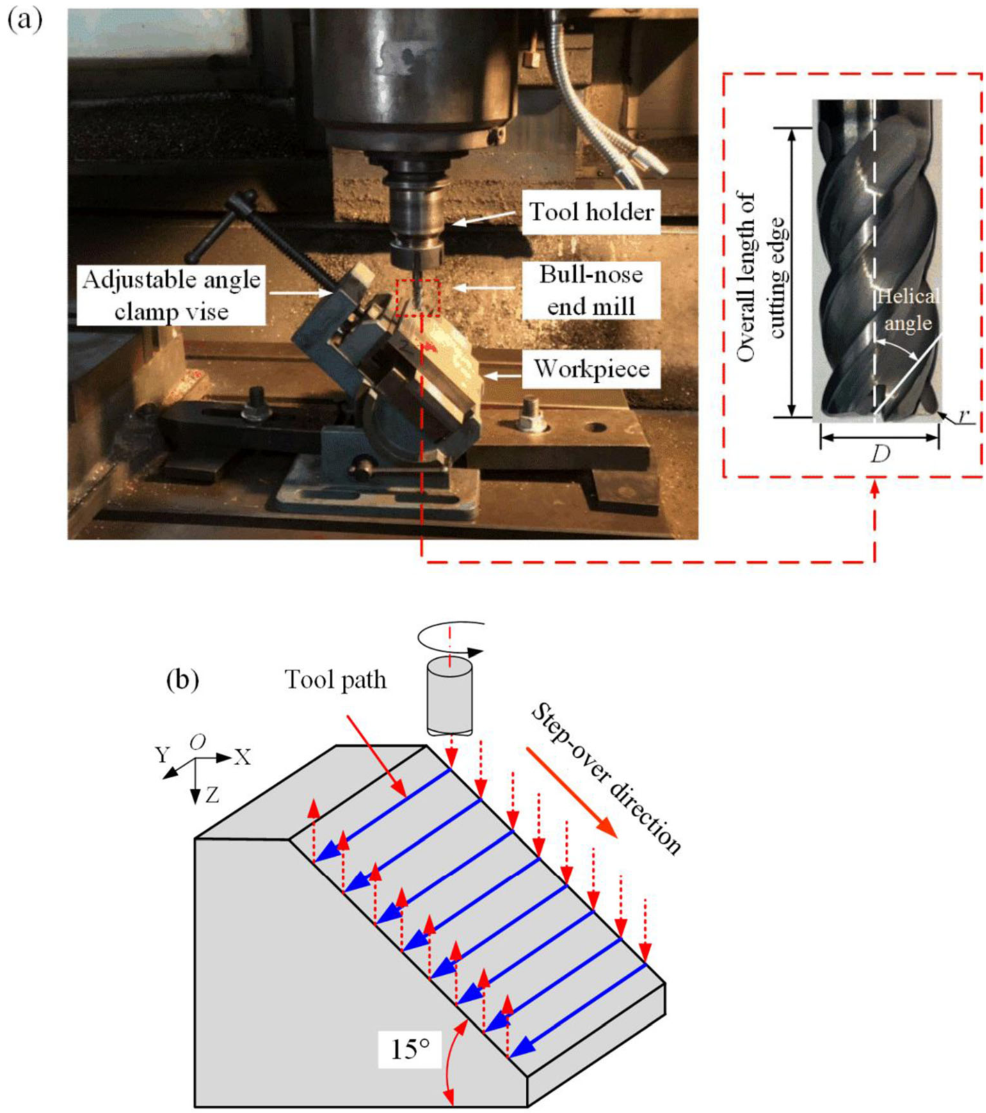

Fig. 4 Schematic diagram of milling tests: **a** experimental set-up and cutting tool, **b** tool path

angle at different heights when the milling cutter with helix angle is used. Since only the fillet-edge of milling cutter is involved in the cutting process, the lag angle of point P in fillet-edge can be calculated by Eq. (4),

$$\psi = \frac{w \tan\gamma}{R(\alpha)} \tag{4}$$

where w represents the coordinate value of point P in tool coordinate system, γrepresents the helix angle of cutter, α is the angle between the OP and W-axis, and ψ is the lag angle of point P. $R(\alpha)$ is the radius of P, which is shown in Fig. 2.

Apparently, the coordinate of P point on cutting edge of integral ball-nose end miller can be obtained through the geometric relationship, as shown in Eq. (5).

$$\begin{cases} u = R(\alpha)cos\psi \\ v = R(\alpha)sin\psi \\ w = r(1{-}cos\alpha) \end{cases} \tag{5}$$

At the same time, it can be seen that

$$R(\alpha) = R{-}r + rsin\alpha \tag{6}$$

Table 1 Chemical composition of P20 steel (wt%)

C	Si	Mn	Cr	Mo	Ni	Fe
0.28~0.40	0.20~0.80	0.60~1.00	1.40~2.00	0.30~0.55	0.05~0.10	Bal.

Table 2 Cutting parameters of milling experiments

Trial no.	Cutting tool specification	v_c (m/min)	a_p (mm)	f_z (mm/tooth)	a_e (mm)
1	*D*8*r*0.5	125.66	0.05	0.48	0.12
2	*D*8*r*0.5	125.66	0.05	0.48	0.16
3	*D*8*r*0.5	125.66	0.05	0.48	0.30
4	*D*12*r*1	169.65	0.05	0.56	0.18
5	*D*12*r*1	169.65	0.05	0.56	0.23
6	*D*17*r*3	186.92	0.05	0.57	0.35
7	*D*22*r*3	241.90	0.05	0.66	0.34

"*D*" refers to diameter of cutting tool; "*r*" refers to corner radius of cutting tool

In addition, for ball-nose end miller with indexable insert, the coordinate of *P* point in cutting edge can be expressed by Eq. (7).

$$\begin{cases} u = r\sin\alpha + R - r \\ v = 0 \\ w = r(1 - \cos\alpha) \end{cases} \tag{7}$$

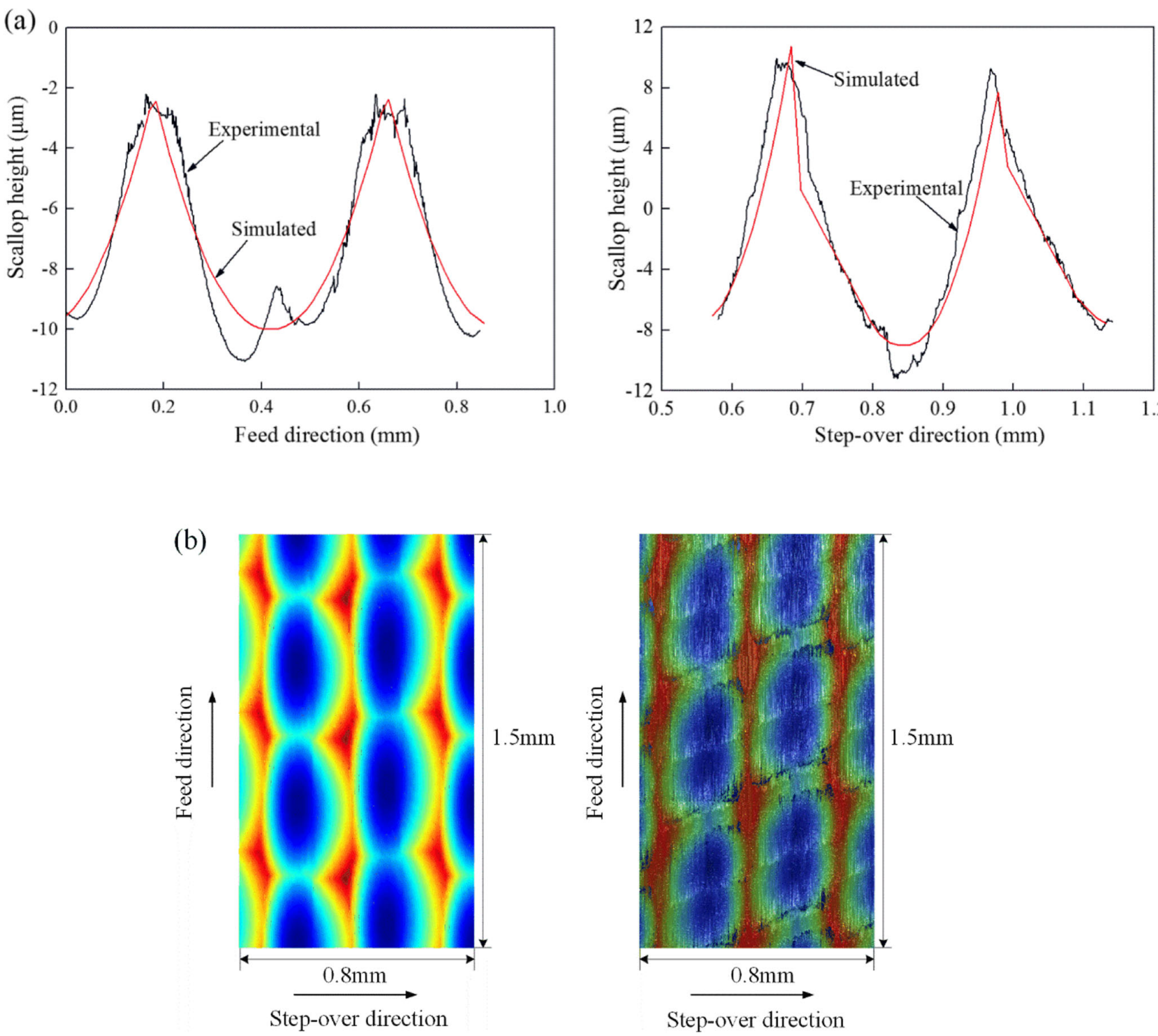

Fig. 5 Comparison between simulated and experimental results at trial no. 3: **a** 2D profiles, **b** 3D surface topography

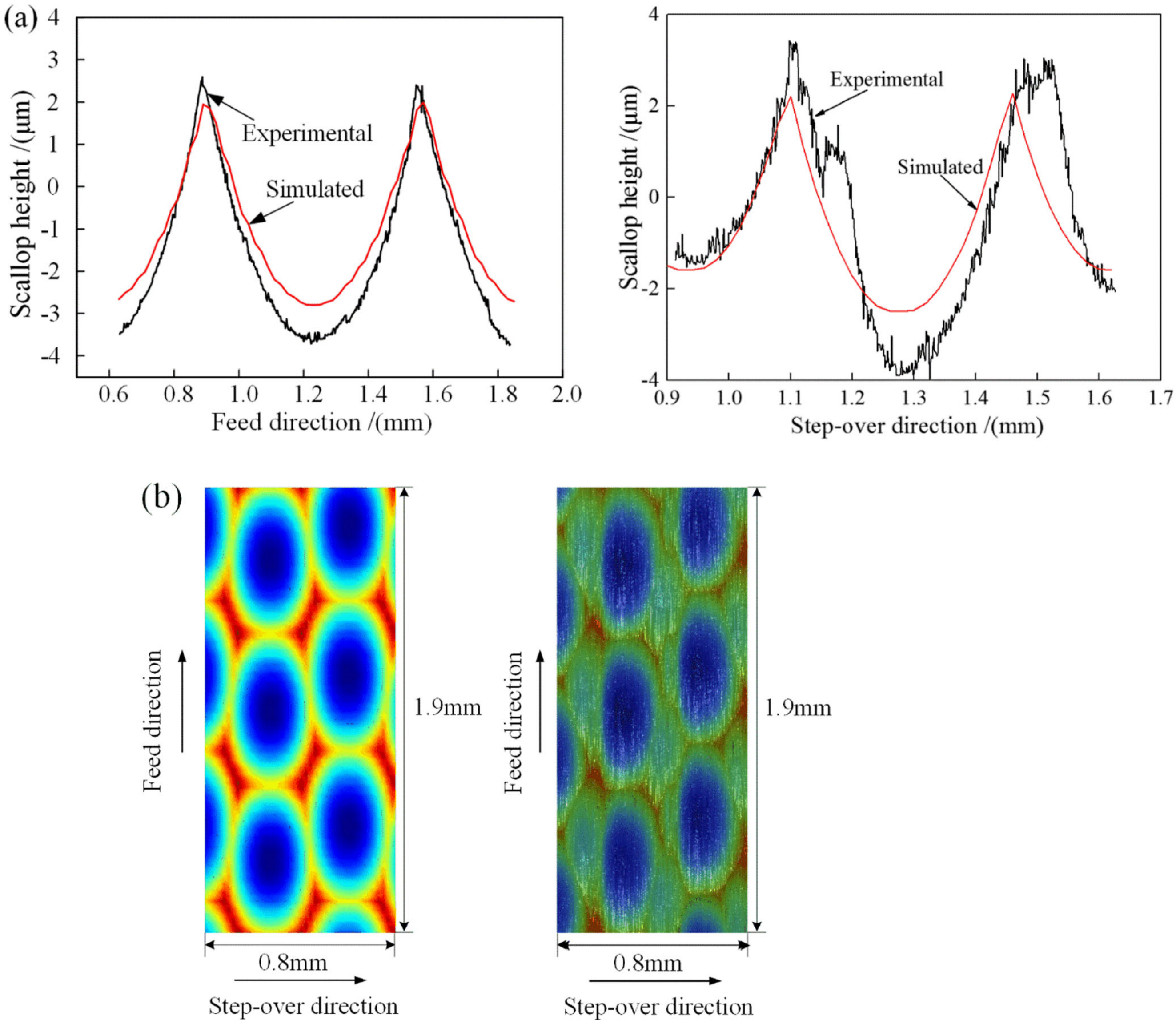

Fig. 6 Comparison between simulated and experimental results at trial no. 7: **a** 2D profiles, **b** 3D surface topography

2.2 Solving algorithm of surface topography

A two-dimensional grid plane model was applied for the workpiece model. As shown in Fig. 3, the workpiece model was divided into $m \times n$ meshes in the workpiece coordinate system, which can be represented by a $m \times n$ zero matrix H. Then calculated the location of discrete cutting-edge point when the tool moves to all discrete tool path position. Next, all z coordinate values of discrete cutting-edge point in each grid are obtained, and the minimum value can be acquired by comparing all values of z in each grid. Finally, the initial value of H will be replaced by corresponding minimum value of z in each grid.

Based on above equations, the minimum z coordinate values of discrete cutting-edge point in each grid can be acquired through calculating the motion track of discrete cutting-edge point in workpiece coordinate system. Then, update the matrix H. according to the new matrix H, the simulated result of surface topography is obtained in MATLAB

Table 3 Comparison between the simulated results and experimental results

Trial no.		1	2	3	4	5	6	7
S_a (μm)	Simulated result	1.85	2.19	4.37	1.77	2.04	1.53	1.58
	Experimental result	1.98	2.51	4.96	1.90	2.31	1.64	1.67
Relative error (%)		6.6	12.7	11.9	6.8	11.69	6.7	5.4

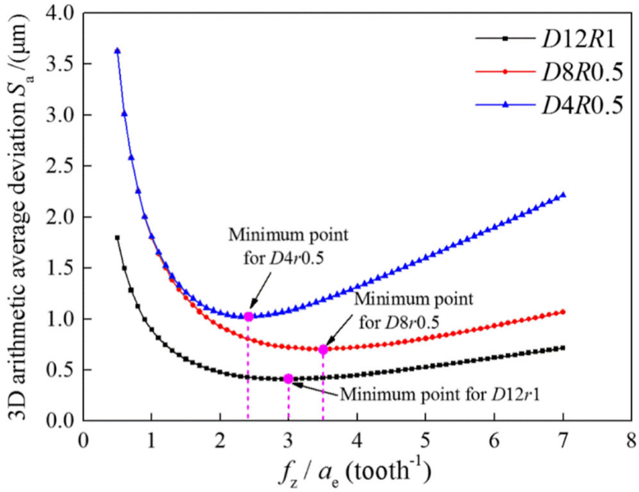

Fig. 7 Relationship curve between S_a and the ratio of f_z and a_e (Note: "*D*" refers to diameter of cutting tool; "*r*" refers to corner radius of cutting tool)

software. Furthermore, the three dimensional arithmetic average deviation (S_a) is also obtained as given in Eq. (8),

$$S_a = \frac{1}{mn} \sum_{x=1}^{m} \sum_{y=1}^{n} \left| h_{xy} \right| \tag{8}$$

where m, n is the number of grids along X, Y direction in workpiece coordinate system, respectively. h_{xy} represents the distance between sampling dot and the mean plane.

2.3 Surface topography model validation

In order to verify the accuracy of surface topography model, the hard milling experiments were performed on a vertical CNC machining center (YCM-V116B). The cutting tools used in experiment were supplied by Seco Tools company. AISI P20 steel was chosen in this research, with the dimension of 100 × 100 × 15 mm. Figure 4 shows the experimental setup and cutting insert. The details of the material and cutting parameters are listed in Tables 1 and 2, respectively. The surface

Table 4 *C* value at different cutting tool specification

Tool specification	*R*/*r*	*C* value
*D*12*r*1	6.0	3.0
*D*6*r*0.5	6.0	3.0
*D*8*r*1	4.0	2.4
*D*4*r*0.5	4.0	2.4
*D*12*r*2	3.0	2.0
*D*6*r*1	3.0	2.0
*D*10*r*1	5.0	2.7
*D*5*r*0.5	5.0	2.7

"*D*" refers to diameter of cutting tool; "*R*" refers to radius of cutting tool; "*r*" refers to corner radius of cutting tool; "*C*" refers to special value of f_z/a_e for obtaining minimum surface roughness

Table 5 *C* values with different values of *R*/*r*

R/*r*	1.0	1.5	2.0	2.5	3.0	3.5	4.0	4.5	5.0	5.5	6.0	6.5
C	1.0	1.3	1.6	1.8	2.0	2.2	2.4	2.5	2.7	2.8	3.0	3.1
R/*r*	7.0	7.5	8.0	8.5	9.0	9.5	10.0	10.5	11.0	11.5	12.0	
C	3.2	3.3	3.4	3.6	3.7	3.8	3.9	4.0	4.1	4.2	4.3	

"*R*" refers to radius of cutting tool; "*r*" refers to corner radius of cutting tool; "*C*" refers to special value of f_z/a_e for obtaining minimum surface roughness

topography of machined surface was measured by white light interferometer (Veeco WYKO NT9300).

The simulated and experimental results at different cutting parameters are shown in Figs. 5 and 6. Figures 5a and 6a show the simulated and experimental results of the transverse 2D profiles taken along the feed direction and step-over direction, respectively. In addition, the simulated and experimental 3D surface topography are also shown in Figs. 5b and 6b. It can be seen from Figs. 5 and 6 that the simulated and experimental results show great consistency. Likewise, according to the comparison of S_a between the simulated and experimental result listed in Table 3, it is obvious that the experimental result for all trials were slightly higher than the predicted result, with relative errors below 13%. Based on Figs. 5 and 6 and Table 3, it supports the fact that the predicting model of surface topography is reliable.

3 Analysis of surface topography model

3.1 Effect of corner radius and diameter of ball-nose end miller on S_a

According to Zhang et al. [23], once the cutting tool and workpiece material are determined, the material remove rate

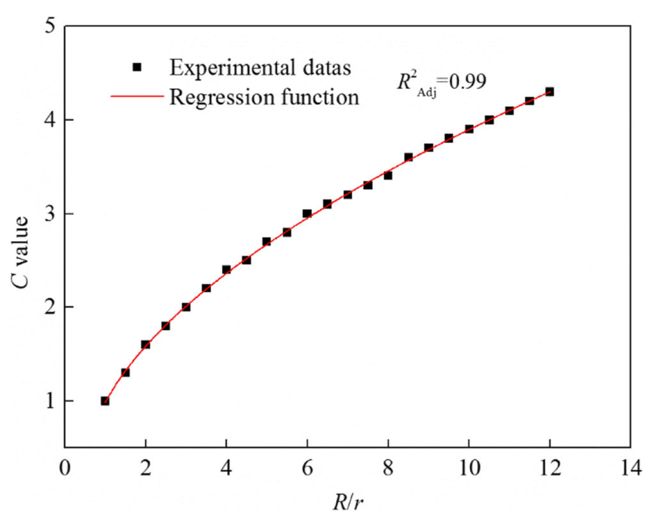

Fig. 8 Analysis of regression function

Table 6 Details and result of validation experiments

Trial no.	Cutting tool specification	$a_e f_z$ (mm^2/tooth)	f_z/a_e (tooth^{-1})	a_e (mm)	f_z (mm/tooth)	S_a (μm)		Relative error (%)
						Simulated	Experimental	
1	*D*10*r*0.5	0.04	3	0.115	0.346	0.96	1.10	12.7
2			3.9	0.101	0.395	0.89	0.98	9.2
3			5	0.089	0.447	0.95	1.10	13.6
4		0.05	3	0.129	0.387	1.20	1.30	7.7
5			3.9	0.113	0.442	1.13	1.26	10.3
6			5	0.1	0.5	1.20	1.34	10.4
7	*D*10*r*1	0.04	2	0141	0.283	0.71	0.77	7.8
8			2.7	0.122	0.329	0.65	0.69	5.8
9			3.6	0.105	0.379	0.70	0.79	11.4
10		0.05	2	0.158	0.316	0.89	0.93	4.3
11			2.7	0.136	0.367	0.81	0.83	2.4
12			3.6	0.118	0.424	0.88	0.92	4.3

"*D*" refers to diameter of cutting tool; "*r*" refers to corner radius of cutting tool

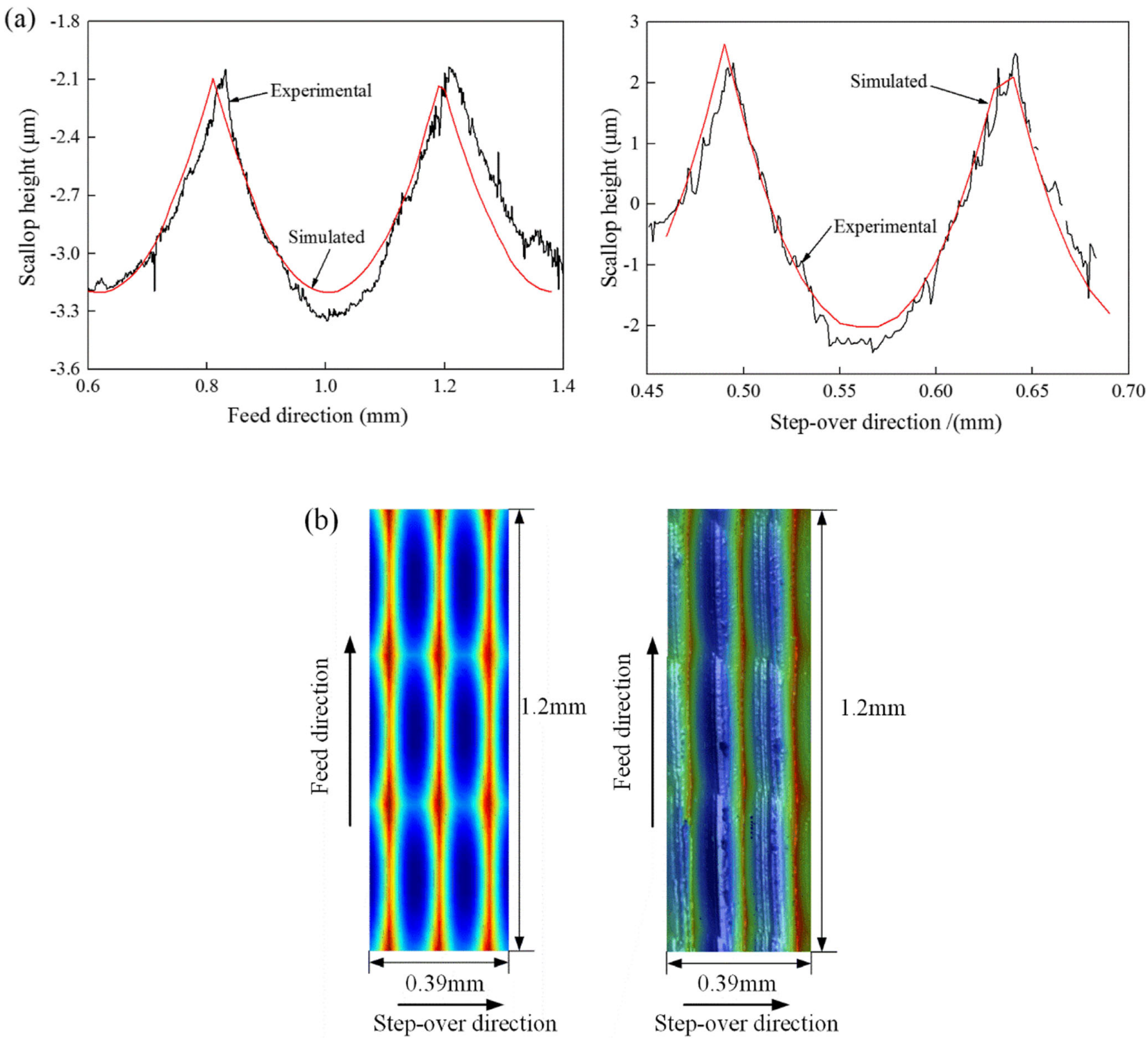

Fig. 9 Comparison between simulated and experimental results at trial no. 4: **a** 2D profile, **b** 3D surface topography

(MRR) is only related to the f_z and a_e. In addition, the f_z and a_e affect the scallop height and geometry both in feed direction and step-over direction, which means different combination of f_z and a_e can cause different surface topography even though the MRR is constant. In the case where the product value of f_z and a_e is constant, the relationship between the S_a and the ratio of f_z and a_e with different cutting tool specification is shown in Fig. 7. It is obvious that the S_a tends to decrease then increase with increasing ratio of f_z and a_e, this indicated that the minimum S_a corresponds to the specific value of the ratio of f_z and a_e which is defined as C. Furthermore, it is noticeable that the minimum point of relationship curve changes with the corner radius and diameter of cutting tool specification shown in Fig. 7, which indicates that better surface topography can be obtained through selecting the suitable f_z and a_e for different cutting tool specification in milling process.

Based on the milling experiments result, the values of C corresponding to minimum S_a in Table 4 show that the C are equal when the ratio of R and r is identical for different ball-nose end miller. Therefore, it means that the C is only related to the ratio of R and r.

In order to reveal the relationship between the C and ratio of R and r, a series of simulated trials are carried out, the results are listed in Table 5. Based on the analysis of frequently used function and simulated results correlation, the exponential function was considered. It can be given by Eq. (9).

$$C = a\left(\frac{R}{r} + b\right)^k + d \tag{9}$$

Where a, b, k, and d are coefficients. The coefficients of regression function are obtained by fitting analysis with the use of simulated trial results. The fitting result is shown in Fig. 8, the relative error is below 5%, furthermore, R^2_{Adj} of regression analysis is equal to 0.99, which indicated that the predicting model is reliable. According to the results of regression analysis, the coefficients of Eq. (9) can be obtained. Consequently, the relationship between the C and the ratio of R and r can be expressed as

$$C = \left(\frac{R}{r} - 0.569\right)^{0.562} + 0.365 \tag{10}$$

3.2 Mathematical model validation

To validate the predicting model (Eq. 10), the experiments employing different tool specification when finish milling inclined AISI P20 steel at a workpiece angle of 15° were carried out. Single direction raster strategy of cutter path orientation was employed in the experiment, as shown in Fig. 4. The details of experiments are shown in Table 6. The cutting tools used in experiment were supplied by Seco Tools company (JHP770100E2R050.0Z4A-SIRA, JHP770100E2R100.0Z4A-SIRA).

Figure 9 shows the simulated and experimental results of the transverse 2D profile and 3D surface topography at trial no. 4 of Table 6, respectively, which also indicates that the surface topography is reliable. In addition, C value of cutting tool with $D10r5$ calculated by Eq. (10) is equal to 3.9 when the minimum surface roughness is obtained, as shown in Table 6, the experimental results indicate that when the ratio of f_z and a_e is equal to 3.9, the surface roughness is minimal, and the C value of cutting tool with $D10r1$ also corresponds to the experimental result. Likewise, the predicted and experimental results show that the relative errors are in the range of 2.4–13.6%. Therefore, it can be concluded that the predicted model (Eq. 10) is reliable and can be used for obtaining desired surface roughness when the cutting parameters are optimized under using ball-nose end millers with different diameter and radius corner.

4 Conclusion

In this research, the surface topography model with considering corner radius and diameter of cutter are developed for ball-nose end milling of AISI P20 steel. The main conclusions that can be derived from this research are summarized as follows:

(1) A predicting surface topography model was established for ball-nose end milling process of AISI P20 steel, the comparison between the simulated and experimental result indicates that the predicting model is reliable.

(2) The effect of corner radius and diameter of ball-nose end miller on surface roughness was investigated, it is observed that the S_a tends to decrease then increase with increasing ratio of f_z and a_e, besides, the special value of C (f_z/a_e) corresponding to minimum surface roughness is related to the ratio of corner radius and diameter of ball-nose end miller.

(3) In terms of minimum surface roughness, a mathematical model is established by taking account of r and D of ball-nose end miller, which indicated that proper selection of cutting parameters (f_z and a_e) with consideration of diameter and radius corner of ball-nose end miller is a novel avenue for acquiring desired surface roughness in ball-nose end milling of AISI P20 steel.

Funding information This work was supported by the National Natural Science Foundation of China (Grants No. 51975333 and No. 51575321) and Taishan Scholar Project of Shandong Province (No. ts201712002).

References

1. Zain AM, Haron H, Sharif S (2010) Prediction of surface roughness in the end milling machining using artificial neural network. Expert Syst Appl 37(2):1755–1768. https://doi.org/10.1016/j.eswa.2009.07.033
2. Tseng T, Konada U, Kwon Y (2016) A novel approach to predict surface roughness in machining operations using fuzzy set theory. J Comput Des Eng 3(1):1–13. https://doi.org/10.1016/j.jcde.2015.04.002
3. Benardos PG, Vosniakos G (2003) Predicting surface roughness in machining: a review. Int J Mach Tools Manuf 43(8):833–844. https://doi.org/10.1016/S0890-6955(03)00059-2
4. Kasim MS, Hafiz MSA, Ghani JA, Haron CHC, Izamshah R, Sundi SA, Mohamed SB, Othman IS (2019) Investigation of surface topology in ball nose end milling process of Inconel 718. Wear 426:1318–1326. https://doi.org/10.1016/j.wear.2018.12.076
5. Bhopale NN, Joshi SS, Pawade RS (2015) Experimental investigation into the effect of ball end milling parameters on surface integrity of inconel 718[J]. J Mater Eng Perform 24(2):986–998. https://doi.org/10.1007/s11665-014-1323-y
6. Gao T, Zhang W, Qiu K, Wan M (2006) Numerical simulation of machined surface topography and roughness in milling process. J Manuf Sci Eng, Transactions of the ASME 128(1):96–103. https://doi.org/10.1115/1.2123047
7. Denkena B, Böß V, Nespor D, Samp A (2011) Kinematic and stochastic surface topography of machined TiAl6V4-parts by means of ball nose end milling. Procedia Eng 19:81–87. https://doi.org/10.1016/j.proeng.2011.11.083
8. Buj-Corral I, Vivancos-Calvet J, González-Rojas H (2011) Influence of feed, eccentricity and helix angle on topography obtained in side milling processes. Int J Mach Tools Manuf 51(12):889–897. https://doi.org/10.1016/j.ijmachtools.2011.08.001
9. Chen M, Chen J, Huang Y (2005) A study of the surface scallop generating mechanism in the ball-end milling process. Int J Mach Tools Manuf 45(9):1077–1084. https://doi.org/10.1016/j.ijmachtools.2004.11.019
10. Erkorkmaz K, Layegh SE, Lazoglu I, Erdim H (2013) Feed rate optimization for freeform milling considering constraints from the feed drive system and process mechanics. CIRP Ann: Manuf Techn 62(1):395–398. https://doi.org/10.1016/j.cirp.2013.03.084
11. Buj-Corral I, Vivancos-Calvet J, Domínguez-Fernández A (2012) Surface topography in ball-end milling processes as a function of feed per tooth and radial depth of cut. Int J Mach Tools Manuf 53(1):151–159. https://doi.org/10.1016/j.ijmachtools.2011.10.006
12. Toh CK (2005) Design, evaluation and optimisation of cutter path strategies when high speed machining hardened mould and die materials. Mater Des 26(6):517–533. https://doi.org/10.1016/j.matdes.2004.07.019
13. Tam H, Cheng H (2010) An investigation of the effects of the tool path on the removal of material in polishing. J Mater Process Technol 210(5):807–818. https://doi.org/10.1016/j.jmatprotec.2010.01.012
14. Chen X, Zhao J, Dong Y, Han S, Li A, Wang D (2013) Effects of inclination angles on geometrical features of machined surface in five-axis milling. Int J Adv Manuf Technol 65(9):1721–1733. https://doi.org/10.1007/s00170-012-4293-y
15. Chen X, Zhao J, Li Y, Han S, Cao Q, Li A (2012) Investigation on ball end milling of P20 die steel with cutter orientation. Int J Adv Manuf Technol 59(9):885–898. https://doi.org/10.1007/s00170-011-3565-2
16. Li SJ, Liu RS, Zhang AJ (2002) Study on an end milling generation surface model and simulation taking into account of the main axle's tolerance. J Mater Process Technol 129(1–3):86–90. https://doi.org/10.1016/S0924-0136(02)00581-2
17. Quinsat Y, Sabourin L, Lartigue C (2008) Surface topography in ball end milling process: description of a 3D surface roughness parameter. J Mater Process Technol 195(1–3):135–143. https://doi.org/10.1016/j.jmatprotec.2007.04.129
18. Surmann T, Enk D (2007) Simulation of milling tool vibration trajectories along changing engagement conditions. Int J Mach Tools Manuf 47(9):1442–1448. https://doi.org/10.1016/j.ijmachtools.2006.09.030
19. Surmann T, Biermann E (2008) The effect of tool vibrations on the flank surface created by peripheral milling. CIRP Annals-Manufacturing Technology 57(1):375–378. https://doi.org/10.1016/j.cirp.2008.0'1.059
20. Arizmendi M, Campa FJ, Fernández J, López de Lacalle LN, Gil A, Bilbao E, Veiga F, Lamikiz A (2009) Model for surface topography prediction in peripheral milling considering tool vibration. CIRP Ann Manuf Technol 58(1):93–96. https://doi.org/10.1016/j.cirp.2009.03.084
21. Toh CK (2004) Surface topography analysis in high speed finish milling inclined hardened steel. Int J Precis Eng 28(4):386–398. https://doi.org/10.1016/j.precisioneng.2004.01.001
22. Wang P, Zhang S, Li Z, Li JF (2016) Tool path planning and milling surface simulation for vehicle rear bumper mold. Adv Mech Eng 8(3):1–10. https://doi.org/10.1177/1687814016641569
23. Zhang Q, Zhang S, Shi W (2018) Modeling of surface topography based on relationship between feed per tooth and radial depth of cut in ball-end milling of AISI H13 steel. Int J Adv Manuf Technol 95(9):4199–4209. https://doi.org/10.1007/s00170-017-1502-8
24. De Souza AF, Diniz AE, Rodrigues AR, Coelho RT (2014) Investigating the cutting phenomena in free-form milling using a ball-end cutting tool for die and mold manufacturing. Int J Adv Manuf Technol 71(9–12):1565–1577. https://doi.org/10.1007/s00170-013-5579-4